





## Research Article

# Identification of fatigue damage evaluation using entropy of acoustic emission waveform

Farhan Tanvir<sup>1,2</sup>  · Tariq Sattar<sup>1</sup> · David Mba<sup>3</sup> · Graham Edwards<sup>4</sup>

Received: 27 June 2019 / Accepted: 14 November 2019 / Published online: 26 December 2019  
© The Author(s) 2019 

## Abstract

Acoustic emission (AE) is a passive nondestructive testing (NDT) technique which is employed to identify critical damage in structures before failure can occur. Currently, AE monitoring is carried out by calculating the features of the signal received by the AE sensor. User-defined acquisition settings (*i.e.*, timing and threshold) significantly affect many traditional AE features such as count, energy, centroid frequency, rise time and duration. In AE monitoring, AE features are strongly related to the damage sources. Therefore, AE features that are calculated due to inaccurate user-defined acquisition settings can result in inaccurately classified damage sources. This work presents a new feature of the signal based on the measure of randomness calculated using second-order Renyi's entropy. The new feature is computed from its discrete amplitude distribution making it independent of acquisition settings. This can reduce the need for human judgement in measuring the feature of the signal. To investigate the effectiveness of the presented feature, fatigue testing is conducted on an un-notched steel sample with simultaneous AE monitoring. Digital image correlation (DIC) is measured alongside AE monitoring to correlate both monitoring methods with material damage. The results suggest that the new feature is sensitive in identifying critical damages in the material.

**Keywords** Acoustic emission · Fatigue damage · Digital image correlation · Structural health monitoring

## 1 Introduction

Acoustic emission (AE) is a passive nondestructive testing (NDT) technique for examining the behavior of materials under stress [1]. It can be defined as a mechanism where materials emit elastic waves when they fail at a microscopic level due to stress. The emitted elastic waves are detected as analog signals using AE sensors. The analog signals are fed to a data acquisition system which digitizes each signal and measures its features (*i.e.*, count, energy, centroid frequency, rise time, duration and peak amplitude). The digitized waveform of the signal and their features can be stored in a computer for post-processing. Figures 1 and 2 highlight the AE working principle and

definitions of the features, respectively. AE has been adopted as an efficient structural health monitoring (SHM) technique as it can provide real-time information regarding the damage location, damage stages and their characteristics. Many other NDT techniques are not able to do this. It has been shown to be successful in monitoring many structures and components [2, 3].

AE features are sensitive to several stages and characteristics of damage in metal such as crack formation/initiation, stable and accelerated crack propagation, brittle fracture, plastic yielding, and twinning and change in fracture mode [4–12]. For example, crack formation in Incoloy 901 has been proven in [5, 6] to be accompanied by a very low count rate. Sinclair et al. [7] showed in a fracture toughness

✉ Farhan Tanvir, santof@lsbu.ac.uk | <sup>1</sup>London South Bank University, 103 Borough Rd, London SE1 0AA, UK. <sup>2</sup>NSIRC, TWI Ltd, Granta Park, Great Abington, Cambridge CB21 6AL, UK. <sup>3</sup>De Montfort University, Gateway House, Leicester LE1 9BH, UK. <sup>4</sup>TWI Ltd, Granta Park, Great Abington, Cambridge CB21 6AL, UK.



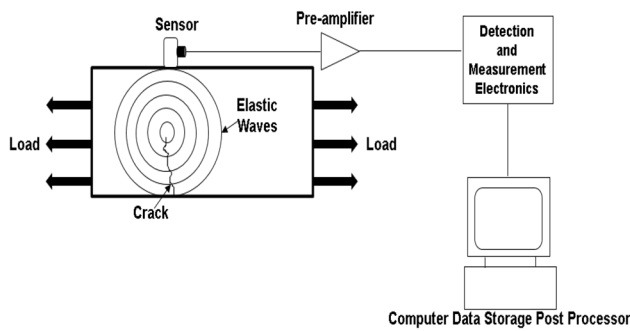


**Fig. 1** AE working principle

test of a wide range of steels (AISI 1060, AISI 1080, SA333 and AISI 304LN) that crack initiation in brittle and ductile material can be correlated with an increase in count and energy.

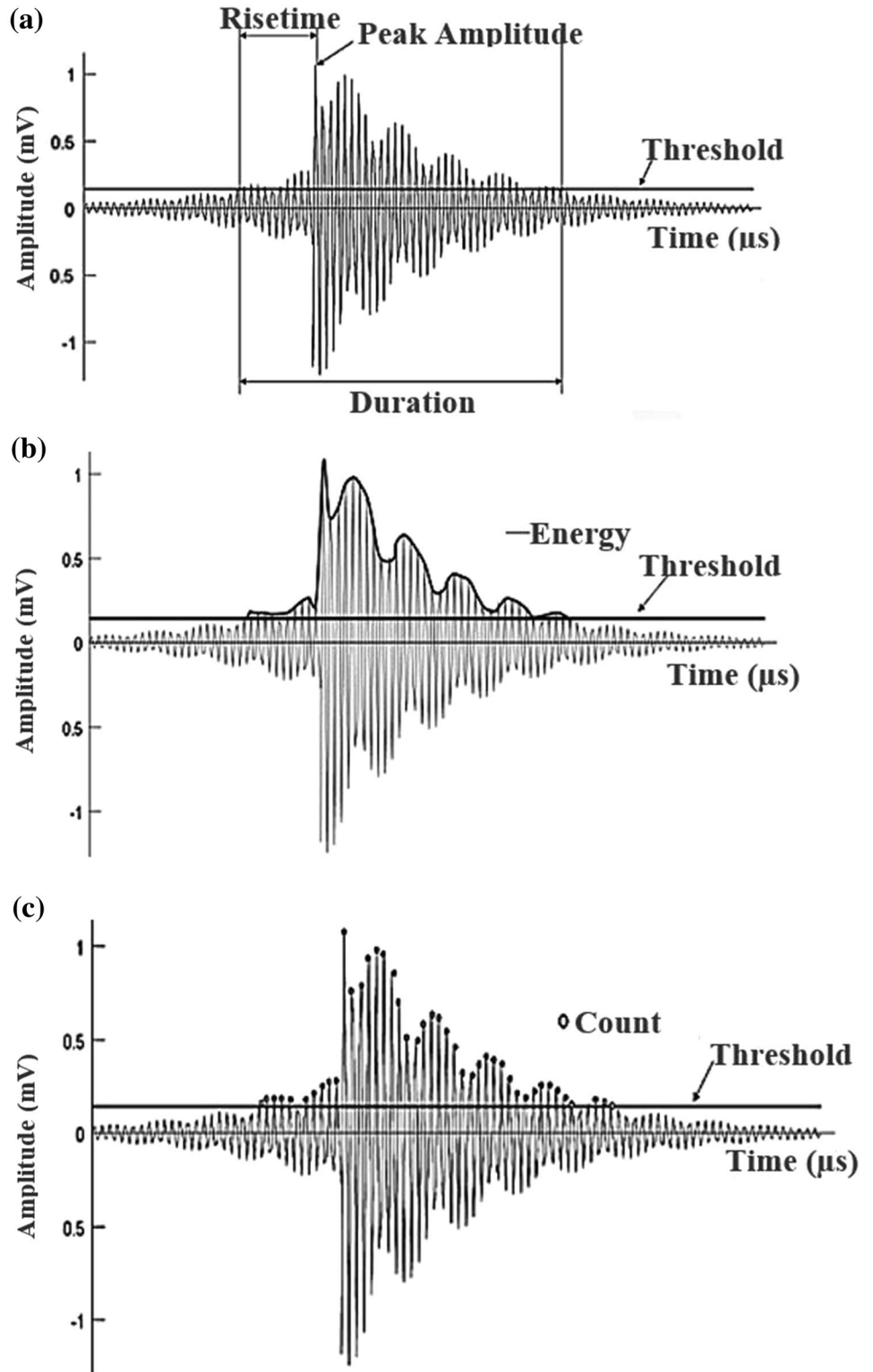
Peak amplitude exhibits a significant increase due to crack initiation in both brittle and ductile materials. Cumulative count in Incoloy 901 and Q345 steel has been shown in [5, 6, 8, 9] to increase steadily during stable crack propagation and rapidly during accelerated crack propagation. Shi et al. [10] showed that the cleavage fractures in R260 steel are correlated with a significant increase in cumulative energy. It has been shown in [11] that damage sources in AZ31 magnesium alloy (*i.e.*, cleavage fracture, twinning, yielding at plastic zone, crack extension and the tear of ligament between micro-cracks and micro-voids) can be distinguished by rise time and peak amplitude observation. Fracture mode changes (*i.e.*, tensile to shear) in Q345 are accompanied by a noticeable increase in rise time and peak amplitude [9]. Fracture mode changes in aluminum (AA 7075) have been shown to have a noticeable increase in duration, rise time and RA value [12]. Robert et al. [13] demonstrated a quantitative approach to estimate crack length based on the count rate of the signals. Despite the reported success of AE, damage identification is still challenging. This is because the current method of analysis for AE monitoring is based on the traditional AE features. AE features are representative of the damage source, and many traditional AE features depend on the user-defined acquisition settings (*i.e.*, threshold and timing). AE features calculated due to inaccurate user-defined acquisition settings will be misleading and can make damage detection difficult. Also, several noise sources may be present during AE data collection, *e.g.*, noise from the loading train,

which may mask the signal generated from the primary AE source.

The aim of this research is to improve the state-of-the-art AE monitoring technique for SHM application. The improved technique is based on a new AE feature to identify damages. It is based on the measure of randomness of the waveform which is calculated using Renyi's entropy. The new feature is based on the fact that the discrete amplitude values of each waveform will have a unique probability distribution and level of randomness. A spreadsheet of a digital waveform shows all the discrete amplitude values including the ones which are well below the threshold. The number of digital values in a transient waveform depends on its page length (*e.g.*, 2500  $\mu$ s) and sampling frequency. In fixed page length settings (FPLS), discrete amplitude values are not strongly dependent on the threshold and timing settings. For example, a burst signal sampled with different settings (*e.g.*, threshold and timing) with a given FPLS (*e.g.*, 2500  $\mu$ s) will have an almost identical waveform and probability distribution. The little difference between them as a result of different thresholds can be explained by the difference in pre-trigger samples. Renyi's entropy computation takes into account all the discrete amplitude values in a waveform (even below threshold). As a result, provided a FPLS is used, it will not be significantly affected by threshold and timing settings. The threshold and timing independence of Renyi's entropy is unlike many AE traditional features. If implemented in AE data acquisition systems, it may improve damage identification. Moreover, computation of entropy uses more information of the waveform than the traditional AE features. The effectiveness of the proposed idea is validated by computing Renyi's entropy of AE signals recorded in 316L stainless steel during fatigue tests and compared with the traditional AE features. Prior to the analysis, AE data is filtered in order to remove unwanted noise. The material behavior (*i.e.*, plastic zone) is correlated with AE activity by using the digital image correlation (DIC) simultaneously with AE monitoring.

The paper is divided into several sections. Section 2 presents the methodology including experimental setup, material, specimen and Renyi's Entropy. In Sect. 3, results of DIC, AE data filtration technique and AE are documented. This section compares the new feature with the traditional features and correlates AE and DIC data. Section 4 addresses the challenges associated with the new feature and suggests future work. Section 5 summarizes the important message of this research.

**Fig. 2** Definition of AE features: **a** rise time, peak amplitude, duration, **b** energy, **c** counts



## 2 Methodology

### 2.1 Experimental procedure

Renyi’s entropy of transient AE waveforms recorded in a sample of 316L stainless steel during fatigue endurance test is computed with a Matlab script. Table 1 shows the mechanical properties of the material used for the experiment. The experimental procedure for the tests was similar to our previous work in Ref. [14]. Two samples were designed using the guidelines of Standard E466-15 and tested at room temperature. The samples were polished with up to 1200 grit emery paper before the test to reduce the stress concentration areas. The 1200 grit provided a mirror finish of the specimens’ surface (which was not achieved with lower grit paper); as a result, the small surface defects were removed. During the test in an Instron machine, the specimens were subjected to sinusoidal loading of 5 Hz and maximum and minimum stress of 480 MPa and 48 MPa.

The elastic waves emitted in the samples were captured as analog signals by a couple of resonant AE sensors (VS-160, resonance range 100–450 kHz) manufactured by Vallen. Figure 3 shows an image of the experimental setup, and Fig. 4 shows a schematic illustration of the fatigue endurance test. The analog signals were amplified with a 34 dB Vallen pre-amplifier. The amplified signals were fed to the AMSY-6 data

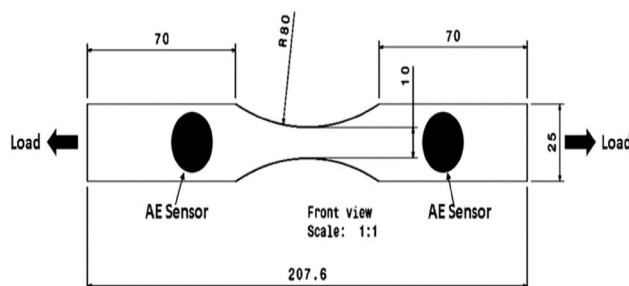


Fig. 4 Specimen dimensions (mm) and test illustration

acquisition system which digitized the signals with a sampling frequency of 5 MHz. After digitization, AE signals were stored as a waveform and their features were calculated. The two ways of recording a waveform are as AE events and as a waveform stream. In a waveform stream, the entire waveform from the start of the test until failure is recorded. A waveform stream is also sometimes called as continuous recording. In AE events, the dominant portion of a waveform stream is recorded as a separate and individual waveform. AE features are then calculated from the individual waveform. The technique records a continuous waveform and requires a significant amount of storage capacity in the hardware. It may be impractical to use this technique if the application requires long-term monitoring. The AE events technique was chosen for this research because it requires much less space to save the data in hardware and at it also retains information regarding the dominant portion of the continuous waveform. Traditional AE features require some user-defined acquisition settings. Therefore, the acquisition settings shown in Table 2 were used for this test.

During AE monitoring of fatigue, several unwanted signals originating from the loading train mask the useful signal and make the interpretation of the results difficult. Therefore, AE signal filtration is an important step in AE monitoring. Several AE filtration techniques for fatigue tests have been proposed in the literature. It has been suggested in [13, 15, 16] that signals originating near the maximum of the load cycle are from material damage. Therefore, signals in the lower load range are considered to be noise and hence filtered out. Pascoe et al. [17] suggested that damage in the material occurs neither at maximum load nor at minimum load in a cycle, but occurs in a segment of the cycle which is above a certain load threshold

Table 1 Mechanical properties of the material

Young’s modulus (GPa)	193 GPA
Yield strength (MPa)	347 MPA
UTS (MPa)	613 MPA

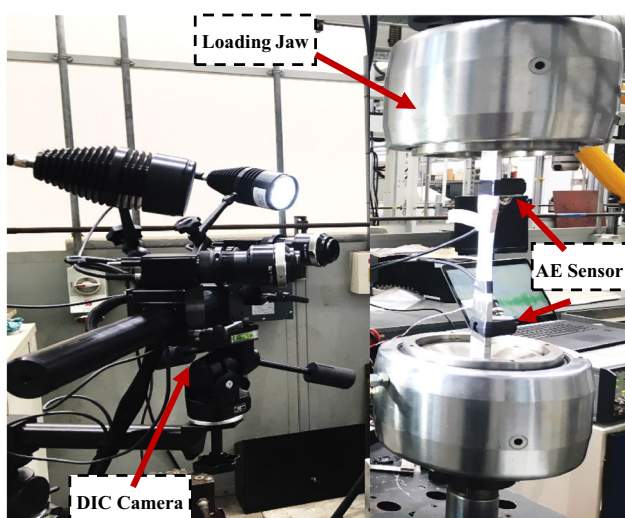


Fig. 3 Experimental setup

Table 2 Acquisition settings

Hit definition time (HDT)	400 μs
Re-arm time	1 ms
Threshold	40 dB
Max duration TR page length	26,214 μs

value. Load threshold value is not a material constant and depends on load history and test frequency. Therefore, the effectiveness of the peak load filtration technique remains questionable. Work performed in Ref. [18] used two filtration techniques. Firstly, a frequency filter eliminated all the transient signals of frequencies below 25 kHz from the data set. Secondly, a count filter eliminated all the transient signals with counts of less than 10. Although these filtration techniques were highly effective, some noise of long duration (10 ms) remained in the data set, which was removed manually. The work performed in [9, 19, 20] used a localization filtration technique to filter out unwanted signals and ensured that the signals were received only from the area of interest. In our work, a 1D localization filtration technique was used to avoid reflections and noise generated at the grips (i.e., loading contact point). The wave velocity chosen for the localization filtration technique was 5000 m/s. It was calculated in 316L stainless steel with the AMSY-6 data acquisition system by pulsing waves from one sensor and receiving the signal with another sensor. The wave velocity calculated by this method is consistent with the asymmetric (A0) wave velocity of 4873.3 m/s and symmetric (0) wave velocity of 4500 m/s below 200 kHz. The reliability of the calculated wave velocity was checked by performing pencil lead breaks (PLB—an artificial damage source) on the surface of the specimen and checking it against the mapped accuracy (i.e., by checking the mapped location in software with the physical location where the pencil lead was broken). The localization results from the PLB test show good agreement with the actual location in the specimen where PLB was performed. This filtration technique considered signals generated within the gauge section of the specimen to be useful and avoided unwanted signals from the grips. To correlate both material behavior and AE activity during the test, the specimens were monitored simultaneously with DIC. The DIC measurement setup was identical to our previous work in Ref. [14].

## 2.2 Renyi's entropy

In physics and mathematics, entropy of a waveform is the measure of information contained in it [21]. Several attempts have been made in the past to successfully measure the entropy of a waveform. Hartley [22] proposed a mathematical model to calculate the total information in a waveform, which was later known as max entropy. Shannon [23] extended Hartley's theory by introducing a weighting function in the calculation, which is recognized as Shannon's entropy. Renyi [24] pointed out that Shannon's entropy restricts the additivity of independent event in a signal to the first (linear) functional class and there exists a second functional class that could also be used. He

developed a continuous family of methods to measure the information in a waveform, by introducing a second (exponential) functional class in the additivity of independent events in a waveform. This computation was regarded as a flexible form of information measure [21] and was later known as Renyi's entropy. Renyi's entropy of a waveform having a random amplitude distribution  $\{x_1, x_2, x_3, \dots, x_n\}$  can be calculated using Eq. (1) as:

$$H_a(x) = \frac{1}{1-a} \log \left( \sum_{k=1}^n (P(x_k))^a \right) \quad (1)$$

where:

The term ' $a$ ' in Eq. (1) represents the order of the entropy and  $P(x_k)$  is the discrete probability distribution of the  $K$ th number of bin.

The most interesting property of Renyi's entropy is its generality because of the choice of ' $a$ ' in Eq. (1). As ' $a$ ' in Eq. (1) increases, more weight is provided to the events with higher probability [25]. A study performed in Ref. [26] suggests more weight is given to the events with high probability when  $a > 1$ , whereas more weight is given to the events with low probability when  $a < 1$ . Depending on the choice of ' $a$ ', Renyi's entropy defines many other forms of entropy, such as:

- When ' $a$ ' approaches 0, it becomes Hartley's entropy or max entropy, shown in Eq. (2).

$$H_0(x) = \log n \quad (2)$$

- When ' $a$ ' approaches 1, the limiting value of  $H(x_k)$  yields Shannon's entropy [27], shown in Eq. (3).

$$\lim_{a \rightarrow 1} H_a(x) = \sum_{k=1}^n P(x_k) \log(P(x_k)) \quad (3)$$

- When ' $a$ ' approaches 2, it becomes quadratic Renyi's entropy, shown in Eq. (4).

$$H_2(x) = \log \left( \sum_{k=1}^n (P(x_k))^2 \right) \quad (4)$$

- When ' $a$ ' approaches infinity, it yields min entropy, shown in Eq. (5).

$$H_{\text{inf}}(x) = -\log \left( \max_k P(x_k) \right) \quad (5)$$

In our research, we have chosen quadratic Renyi's entropy ( $a = 2$ ) for measuring the information contained in a AE waveform because of two reasons. Firstly, the contribution of events with large probabilities is higher in entropy computation than that of events with lower

probability. Therefore, it becomes reasonable to emphasize more on the events with higher probabilities by choosing  $\alpha > 1$ . On the other hand, choosing a higher value of 'a' would significantly weaken the contribution of events with smaller probability. Considering this trade off,  $\alpha = 2$  provides an optimum solution because it provides more weight to the events with higher probability and it is close to Shannon's entropy and thus contains information on all probability events. Secondly, quadratic Renyi's entropy has significant computational advantage compared to any other measures of entropy. By using the Prazen window and kernel, it can be estimated directly from the random amplitude distribution  $\{x_1, x_2, x_3, \dots, x_n\}$  very quickly, bypassing the need to accurately measure the probability distribution [28–30]. This may reduce the computation time of entropy if the Prazen window and kernel density is implemented in an AE data acquisition system.

There are a number of methods to generate the discrete probability distribution [31–33]. In our previous work [14], discrete probability distribution was generated by considering the original spectrum of the waveform. This technique has been widely used in signal processing [34, 35]. Discrete probability distribution in the research performed in [36, 37] was based on the frequency of occurrence with a bin width. A comparison between these two techniques in Ref. [32] suggests that an entropy computation by considering the probability distribution with frequency of occurrence and a bin width to be more reliable than the original spectrum of the signal. In this work, entropy was computed by taking into account the probability distribution with frequency of occurrence and a bin width of 0.00305 mV. In order to measure the signal entropy in bits, the base of the log was chosen to be 2. This research will refer to quadratic Renyi's entropy of transient AE waveform as AE entropy. The following steps demonstrate the AE entropy calculation procedure.

*Step 1* AE waveforms recorded by the AMSY-6 data acquisition system were copied into a spreadsheet containing the amplitude distribution values (Table 3).

*Step 2* The spreadsheet containing the amplitude distribution values were imported into Matlab. Discrete probability distribution of the amplitude sequence was then generated using a bin width of 0.000153 mV (see Fig. 5).

*Step 3* From the discrete probability distribution, calculation of AE entropy was accomplished by Eq. (1). AE

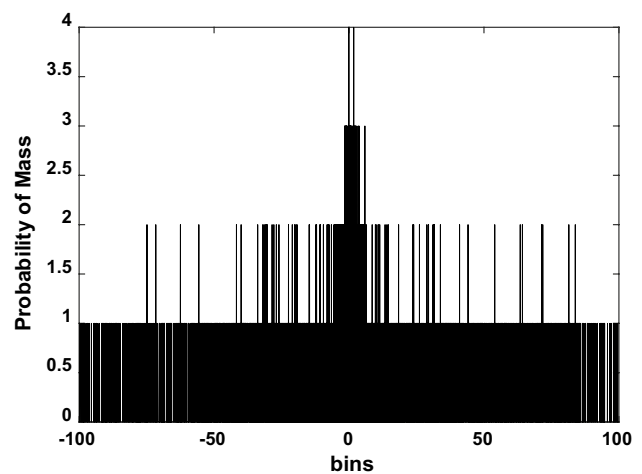


Fig. 5 Entropy computation step 2

entropy of the discrete amplitude distribution in Fig. 5 was found to be 8.3. This value represents the degree of disorderness in the discrete amplitude distribution and is the average number of bits required to store it. The larger the disorderness in discrete amplitude distribution, the larger will be the average number of bits required to store it.

### 3 Results

#### 3.1 Digital image correlation (DIC)

The DIC measurement and AE data were synchronized by starting the DIC camera and AE data acquisition system at the same time, such that they start capturing data simultaneously. There were several images taken by the DIC camera during the entire length of the test. Figure 6 highlights a few important images of strain map ( $\epsilon_{yy}$ ) taken by the DIC for test 1. Figure 6a shows the reference image; this image was taken before the onset of loading. The image in Fig. 6b was taken at 10,000 s after the onset of loading, and it can be observed in this image that strain maximizes at the middle of the gauge section. The image in Fig. 6c at 21,556 s does not show any difference from the image in Fig. 6b. This suggests that the surface strain remains stable within this time. The image in Fig. 6d at 22,911 s shows that the strain concentrates at the edge of the specimen forming a plastic zone (marked by a black arrow). The plastic zone at this point is likely due to significant formation and coalescence of a micro-crack. This phenomenon is explained in Ref. [38]. The image in Fig. 6e at 23,250 s shows an increase in the plastic zone area found at the edge of the image in Fig. 6d (marked by a black arrow). The image in Fig. 6f at 23,590 s shows that the plastic zone area becomes clearly highlighted (marked by a black arrow). The image in Fig. 6g shows a macro-fatigue crack initiation

Table 3 Entropy computation step 1

$X_1$	-0.88291329
$X_2$	-0.71850872
...	...
$X_{3899}$	4.9595370
$X_{3900}$	-5.4953742

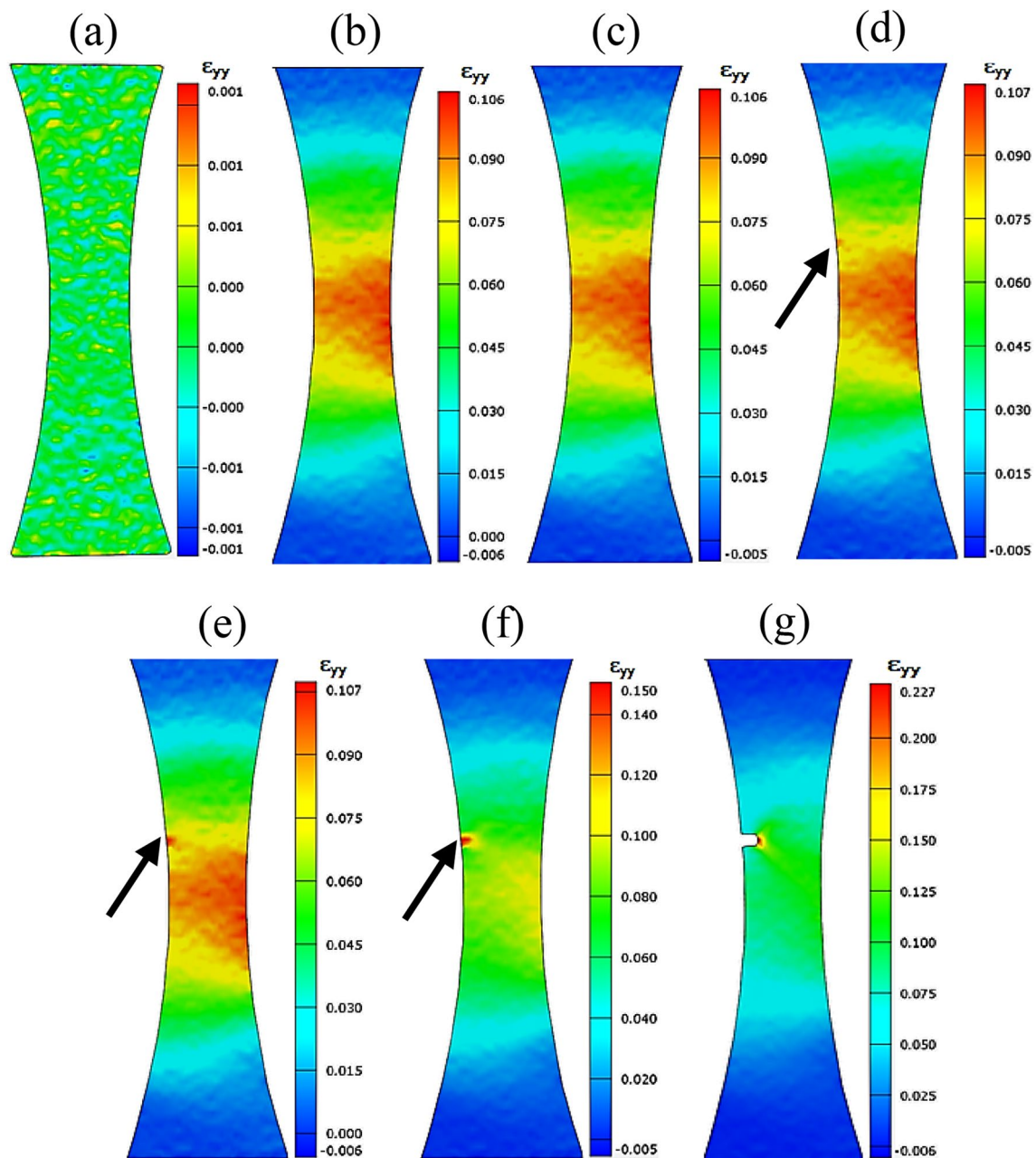


**Fig. 6** DIC images test 1: **a** reference stage, **b** at 10,000 s, **c** at 21,556 s, **d** at 22,911 s, **e** at 23,250 s, **f** at 23,590 s and **g** at 23,928 s

from the plastic zone formed earlier. The time instance of plastic zone localization and macro-crack initiation will be cross-validated with AE activity.

Figure 7 shows a few important images of strain map ( $\epsilon_{yy}$ ) taken by DIC for test 2. The image in Fig. 7a shows the reference image taken before the onset of loading. The image in Fig. 7b was taken 10,000 s after the onset of loading. Like the image in Fig. 6b, the image in Fig. 7b also shows strain maximization at the center of the gauge section. The image in Fig. 7c at 23,636 s does not show any difference from the image in Fig. 7b. This suggests that there is no change

in surface strain within this time. The image in Fig. 7d at 25,084 s shows slight changes in the strain map of the gauge section as compared to the image in Fig. 7c. The image 7e at 25,265 s shows two strain concentrated areas (marked by black arrows). The formation of two strain concentrated areas could be a result of the plastic zone formed by the crack initiation on the other side of the specimen, which is not covered by the DIC camera. This is very likely because the thickness of the specimen was very small (2.5 mm). The formation of two strain concentrated areas becomes very evident in the image in Fig. 7f at 25,446 s (marked by black arrows). The image in

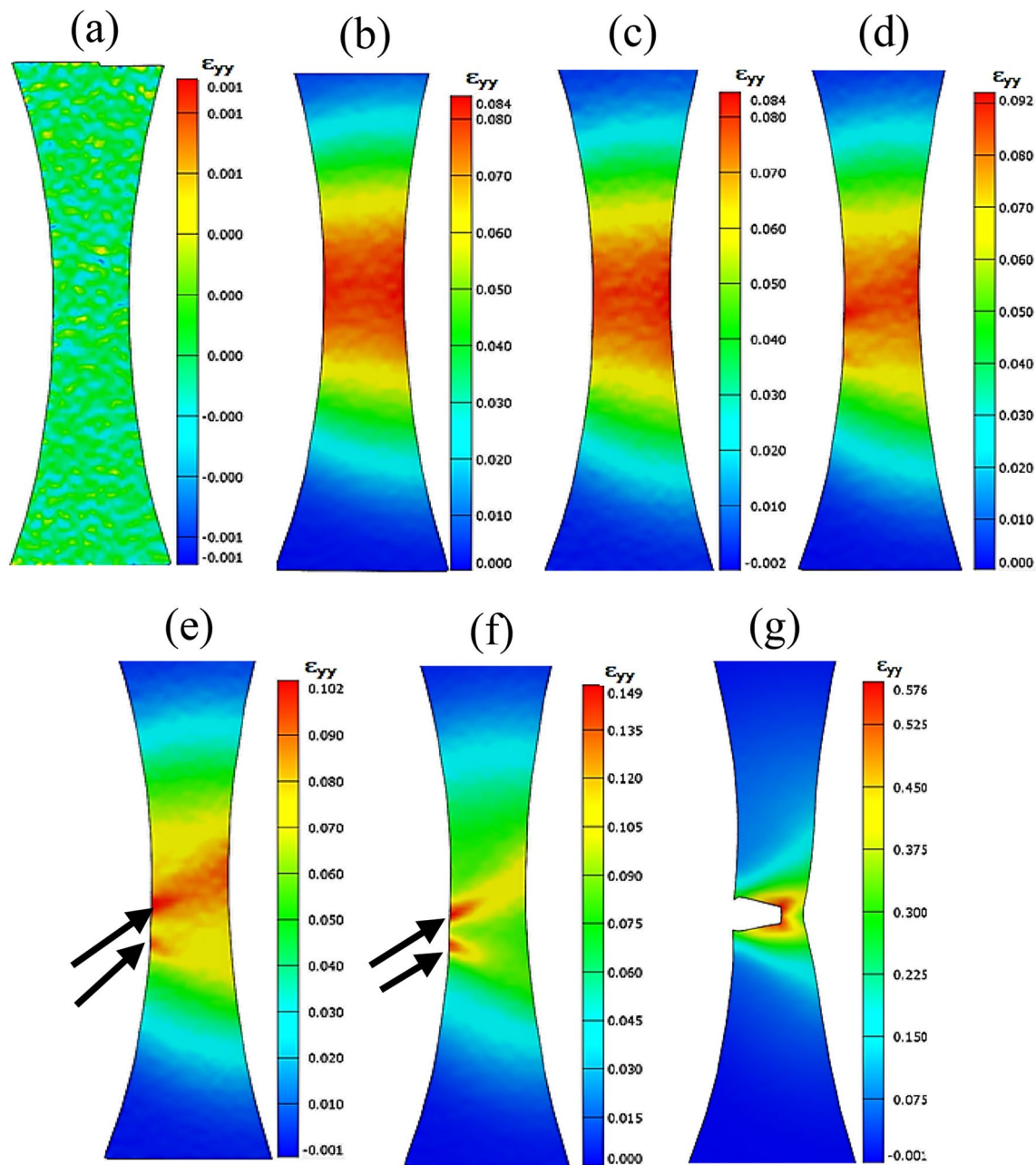


Fig. 7 DIC images test 2: **a** reference stage, **b** at 10,000 s, **c** at 23,636 s, **d** at 25,084 s, **e** at 25,265 s, **f** at 25,446 s and **g** at 25,627 s

Fig. 7g at 25,627 shows a crack initiation from the middle of the two strain concentrated areas. The time instance of the strain concentration will be cross-validated with AE activity.

### 3.2 Acoustic emission data filtration

Figure 8a, c shows the unfiltered data of cumulative count for tests 1 and 2, respectively. It is mentioned in [5, 6, 39] that cumulative trend remains stable in the early stages and increases at the later stages of fatigue. It can be

observed in these figures that no typical trend as mentioned in [5, 6, 39] can be identified in these plots. 1D linear localization filtration technique mentioned in Sect. 2.1 was applied to these unfiltered data sets. Figure 8b, d shows the cumulative count plot of the filtered data for tests 1 and 2. It can be observed in Fig. 8b, d that the cumulative count begins to increase during the later stage of test and is consistent with the observations of other researchers [5, 6, 39]. The trend observed in these plots will be discussed in detail later in Sect. 3.3. It can be concluded



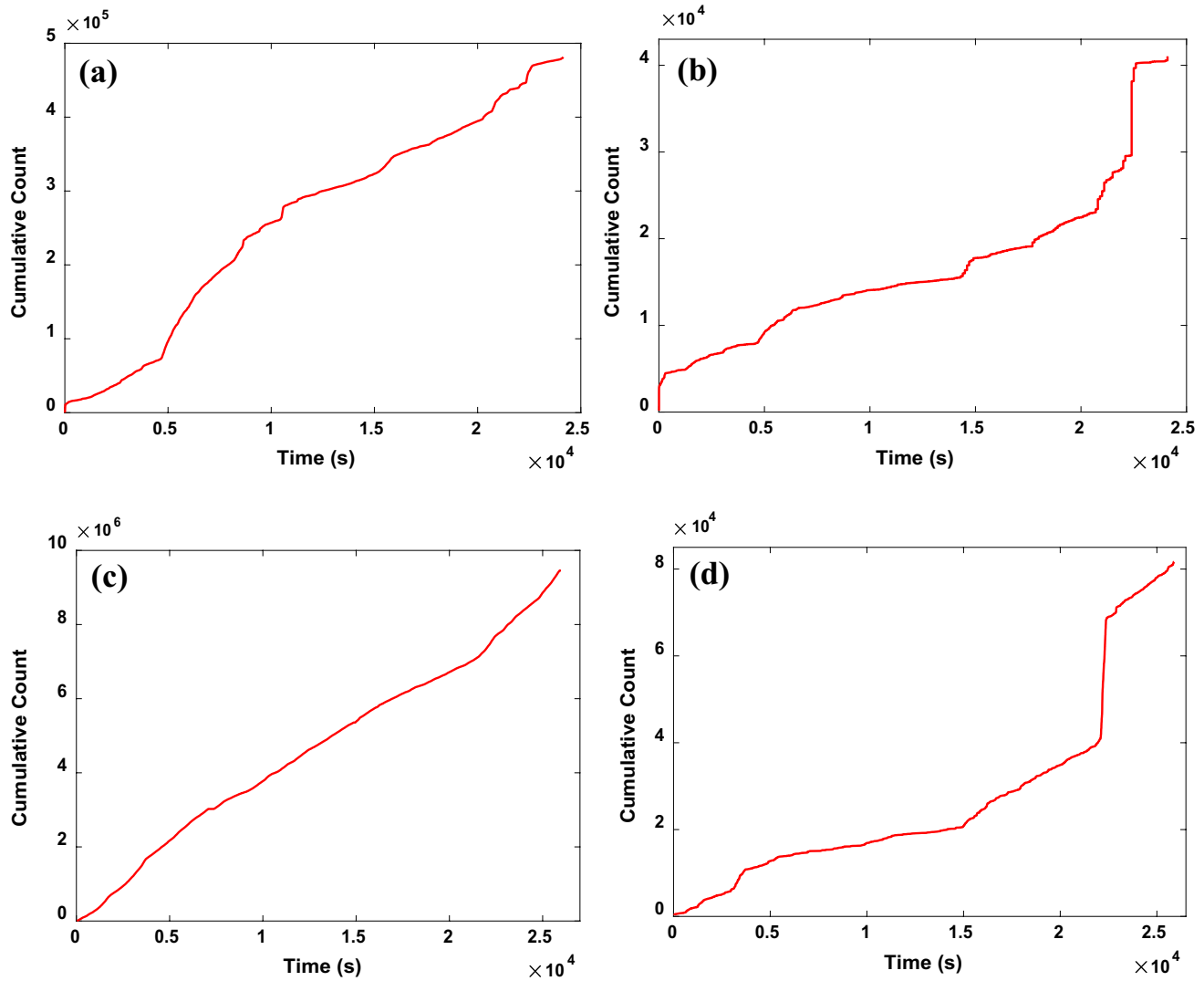


**Fig. 8** **a** Test 1 unfiltered data. **b** Test 1 filtered data. **c** Test 2 unfiltered data. **d** Test 2 filtered data

that the filtration technique had a significant effect in denoising the data because the filtered data of cumulative count possess the same trend as those mentioned in the literature. After the noise filtration, AE entropy was computed on the remaining data set and compared with the traditional AE features.

### 3.3 Comparison of traditional AE analysis with AE entropy

To investigate the performance of AE entropy, it is crucial to understand the damage mechanism and its corresponding AE activity. At the onset of loading, AE activity is generally higher due to yielding of the material as a result

of the change in stress state. After the onset of loading AE activity is lower, this stage is regarded as the damage incubation stage. At the end of this stage, AE activity increases significantly as a result of growth and coalescence of a micro-crack initiated in the earlier stage. These trends have been validated in Refs. [5, 6, 39]. When the growth and coalescence become concentrated in an area, it gives rise to a plastic zone in the material.

Fatigue studies using AE are mostly based on the cumulative analysis of energy and count [6, 8, 20, 40]. Therefore, the cumulative trend in AE entropy was compared with these features in Figs. 9 and 10 for tests 1 and 2, respectively. It is clear from Figs. 9 and 10 that cumulative entropy and cumulative count exhibit the same trend during the entire fatigue

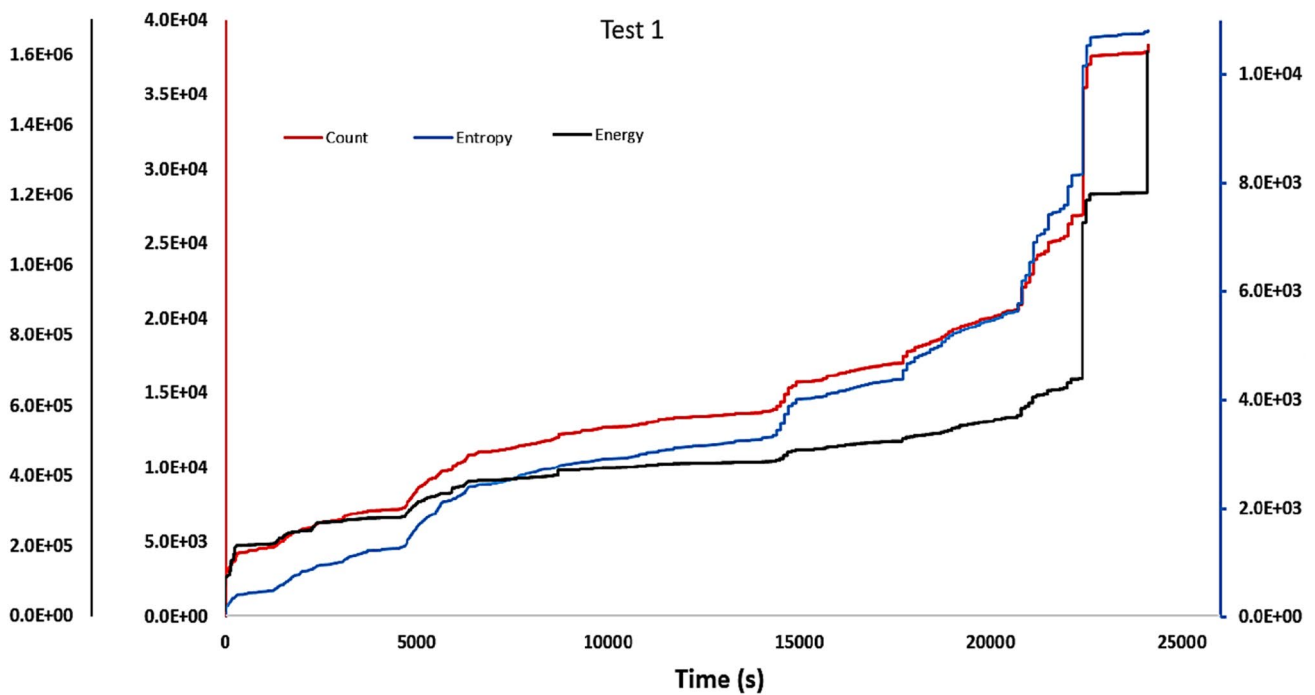


Fig. 9 Comparison of cumulative features (test 1)

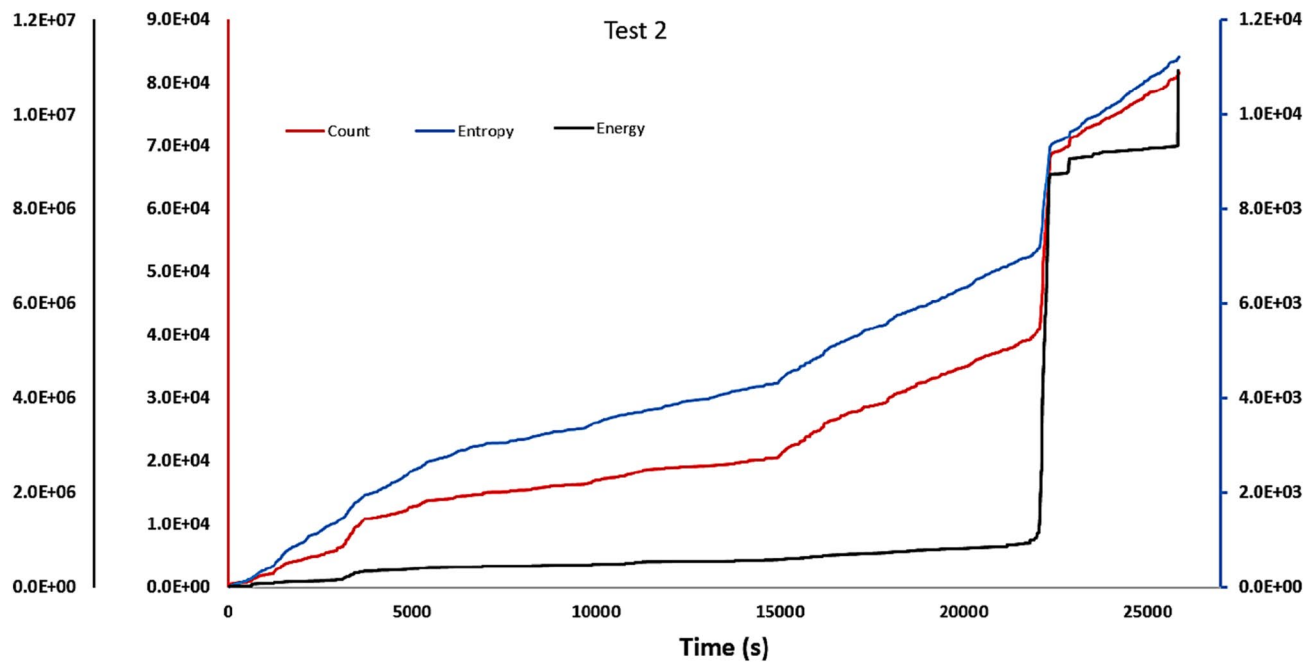


Fig. 10 Comparison of cumulative features (test 2)

test. It can be observed in Fig. 9 that at around 23,000 s, there is a significant jump in all the cumulative features. This time is associated with the plastic zone formation in the DIC images shown in Fig. 6 (for test 1). Therefore, it can be concluded that the significant jump in AE activity is an indicator of plastic zone formation. Figure 9 shows that cumulative features

(especially count and entropy) begin to increase slightly after 15,000 s and noticeably after around 20,000 s. DIC images in Fig. 6 do not show any change in surface strain until 21,556 s. The noticeable increase in cumulative features from around 20,000 s could be as a result of growth and coalescence of a micro-crack, before it manifests into plastic zone formation.

Therefore, it can also be concluded that AE is more sensitive than DIC for damage identification. The merit of the sensitivity of AE over other NDT techniques has been shown by other researchers [8, 12]. Figure 10 shows a comparison of traditional cumulative features with cumulative entropy for test 2. Figure 10 shows that there is a significant jump in all the cumulative features at around 22,500 s. No significant changes can be observed in the DIC images during this time in Fig. 7; in fact, no significant changes are observed in the DIC images until 25,265 s. At 25,265 s, DIC images in Fig. 7 show two distinct strain concentration areas which becomes clearer at 25,446 s. The significant jump in Fig. 10 at around 22,500 s could be attributed to plastic zone formation on the other side of the specimen which is not covered by the DIC camera. Cumulative parameters (especially count and entropy) begin to increase noticeably from around 15,000 s, and this could be attributed to growth and coalescence of a micro-crack.

It is evident from Figs. 9 and 10 that there is a noticeable difference in the cumulative trend between AE entropy and energy. In both tests, cumulative entropy begins to increase noticeably before the damage manifests into plastic zone formation and significantly at the onset of plastic zone formation, whereas, in neither of the tests, there is a noticeable increase in cumulative energy before plastic zone formation. In fact, cumulative energy is sensitive only at the formation of plastic zone and ultimate fracture of the specimen.

The observed difference in trend is due to the nature of the respective feature extraction processes. Energy is the area under the waveform, and plastic zone formation and fracture is accompanied by waveforms with significantly higher energy than the other stages. The sudden burst of events and a few highly energetic waveforms at fracture masks the collective cumulative trend in energies prior to the plastic zone formation. In the case of AE entropy, the spread in the data (individual AE events) used to construct the cumulative trend is significantly lower than that of cumulative energy. For instance, the spread in data points used to construct cumulative entropy is 0–10 bits, whereas for cumulative energy it is 0– $401 \times 10^3$  eu. Although AE events at fracture are associated with high AE entropy, there is no significant jump observed in the cumulative entropy plot. A few high AE entropy events at fracture are not able to produce a jump in the cumulative plot due to the lower spread in the data.

To investigate fatigue damage evolution, a single cumulative feature cannot solely be used, because of the varying degree of sensitivity of each cumulative feature in different stages of fatigue. As a result, both cumulative count and cumulative energy have been used together in many fatigue tests. It is evident from Figs. 9 and 10 that cumulative count and entropy curves show the same trend. The similar increasing trend in cumulative count and entropy shows the feasibility and effectiveness of cumulative entropy as

a damage identification feature. Unlike cumulative count, cumulative entropy is independent of user-defined acquisition settings. This can reduce the need for human judgement in measuring the feature of the signal. Therefore, in the future, entropy has the potential to replace count in AE monitoring.

## 4 Discussion

The formation of a plastic zone facilitates macro-fatigue crack initiation. These fatigue cracks can propagate and lead to an ultimate failure of the material. Therefore, identifying the formation of a plastic zone is an indication of a critical stage of damage in a material. The results show that AE entropy, like the traditional features, is sensitive in identifying the onset of plastic zone formation in the material. Although AE entropy has the same trend as count and energy, it is independent of acquisition settings (unlike many traditional AE features) provided a FPLS setting is used. In order to investigate the effect of acquisition settings such as threshold on the AE entropy, the filtered signals were analyzed by considering three distinct threshold settings. Figures 11 and 12 show the total cumulative AE entropy and count versus each threshold setting for test 1 and test 2, respectively. It can be observed in these

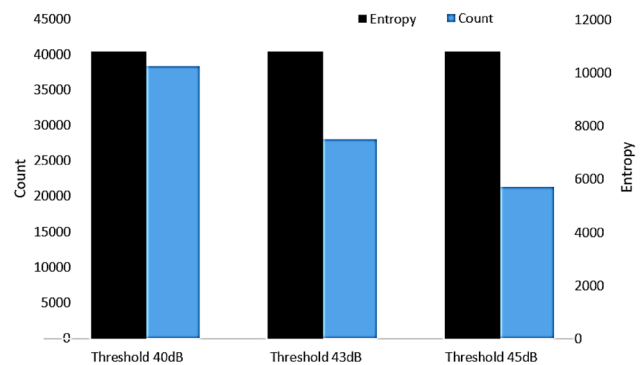


Fig. 11 Comparison of cumulative features

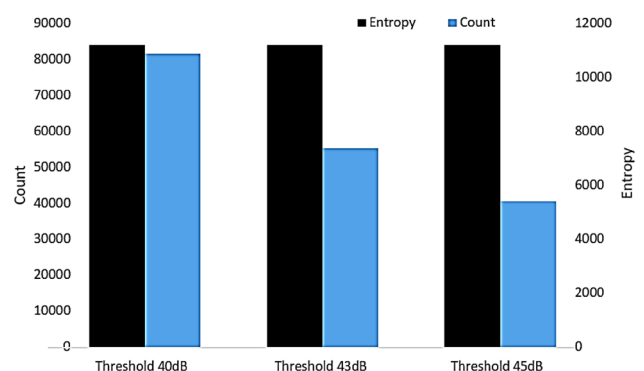


Fig. 12 Comparison of cumulative features

figures that as the threshold increases, the total AE count decreases, whereas the entropy remains constant. The threshold independence of AE entropy is due to its computation which takes into account of all the possible discrete voltage values in each waveform.

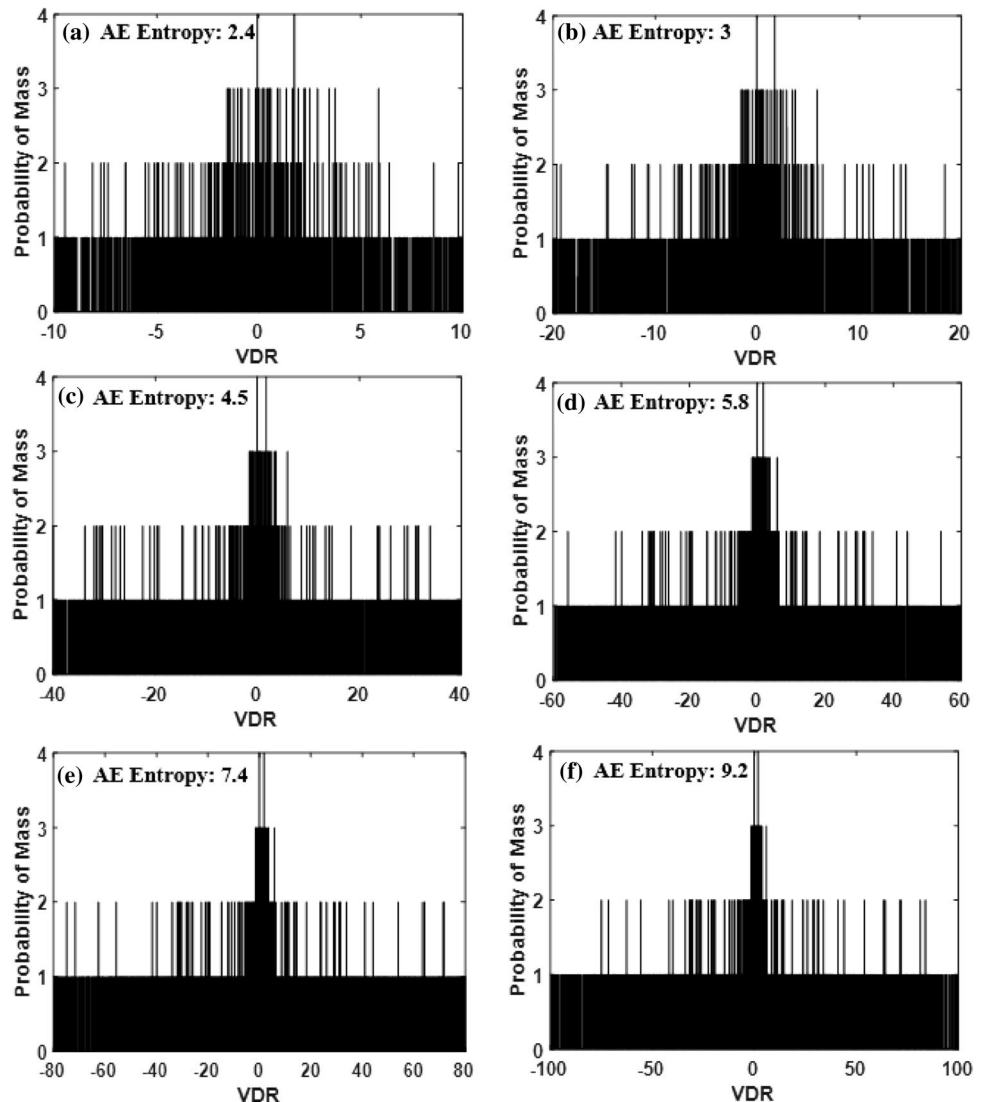
In contrast, computation of the AE count relies only on peaks above the threshold. AE entropy has the potential to be implemented in commercial data acquisition systems as it can provide valuable condition monitoring indication of damage in structures during operation and maintenance, with reduced reliance on human judgement to set AE acquisition settings. However, there are some aspects to be addressed while performing AE entropy computation, particularly the voltage distribution range and bin width.

Firstly, the voltage distribution range (VDR) is an important aspect to consider while performing AE entropy computation. VDR is the range of voltages over which

probability distribution is calculated. Ideally, VDR should be set by taking into account the highest and lowest voltage values of the highest peak amplitude signal in the dataset. However, it is not possible to predict these values prior to the experiment. Therefore, VDR of  $-100$  to  $+100$  mV was chosen for these experiments, which is equal to the maximum limit of voltage range in an AE data acquisition system for transient waveform recording. Insufficient VDR can result in an inaccurate computation of AE entropy.

Figure 13 shows the effect of VDR on the calculated AE entropy of a waveform captured during the tests. It can be observed in graph (a) of this figure that VDR of  $-10$  to  $+10$  restricts the probability distribution of the voltages from  $-10$  to  $+10$  mV and results in an AE entropy of 2.4. It can be observed in graphs (b) (c), (d), (e) and (f) that with increasing VDR, the AE entropy also increases. It is also evident that the AE entropy in graph (f) is almost four time

**Fig. 13** Effect of voltage distribution range on AE entropy: **a** VDR  $-10$  to  $10$ , **b** VDR  $-20$  to  $20$ , **c** VDR  $-40$  to  $40$ , **d** VDR  $-60$  to  $60$ , **e** VDR  $-80$  to  $80$  and **f** VDR  $-100$  to  $100$



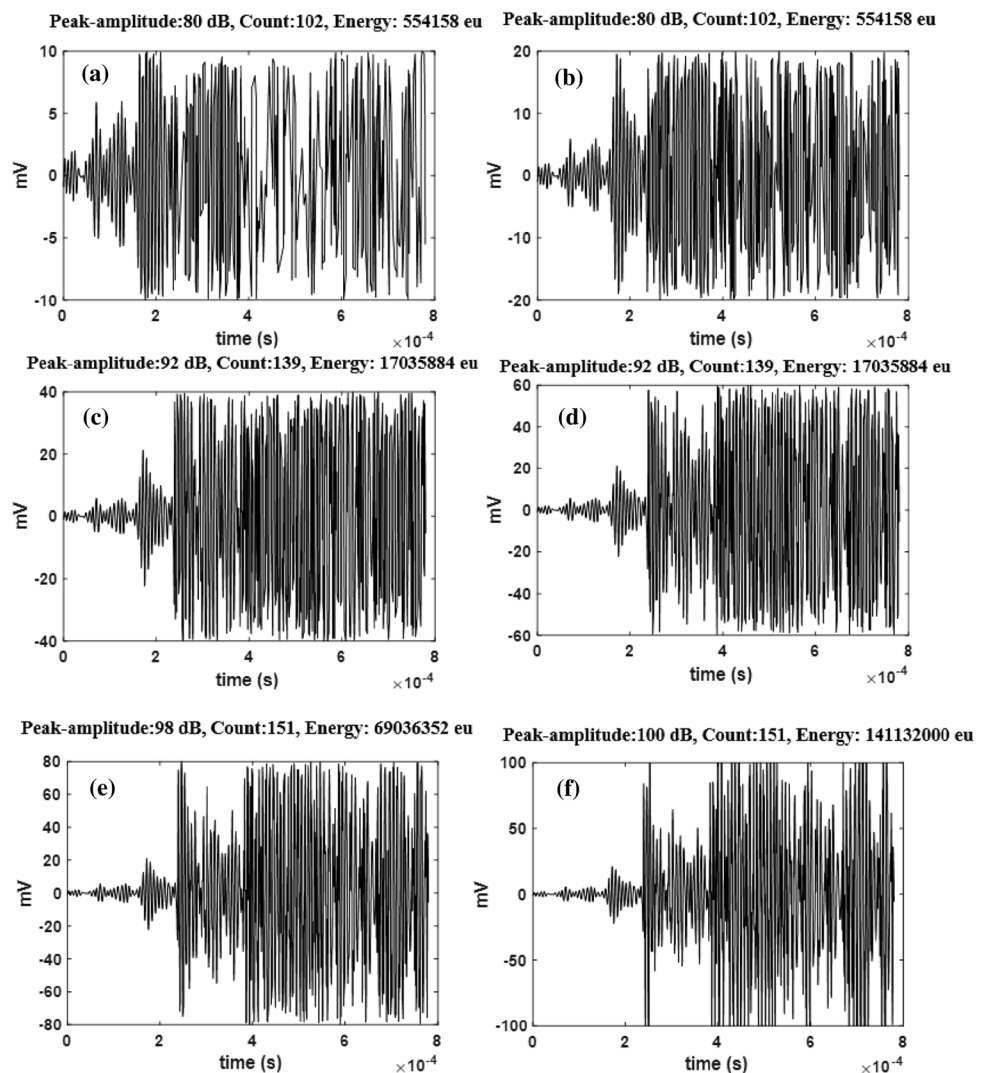
that in graph (a), although both the graphs correspond to the same waveform. This increase in AE entropy with VDR is due to the increase in available probability of mass of the voltage. Like the effect of VDR on AE entropy, the traditional features are also affected by the maximum limit of the voltage range in the waveform. Figure 14 shows the waveforms, with a series of maximum limits of the voltage range, equivalent to each of the VDR in Fig. 13. Each graph in Fig. 14 contains some of its traditional features. It is evident from this figure that with the maximum limit of the voltage range, the traditional features of the waveform increase. This can be attributed to the additional voltage values at the higher limit of the voltage range. Unlike the acquisition setting, the maximum limit of the voltage range is not a user input parameter. In other words, the traditional features are always calculated from a built-in voltage range. Therefore, in every situation the traditional features are going to be extracted from the same voltage range. If AE entropy is implemented in the AE data

acquisition system, the VDR can always be set equal to the built-in maximum limit of the voltage range. By doing this, the VDR will also be implemented as a built-in range rather than a user input parameter.

Secondly, the choice of bin width to generate the discrete probability distribution is also of great importance. If the bin width is too large, there will be too many samples within each bin and the disorderness of the probability distribution will be lost. If the bin width is too small, there will be too few samples within each bin and the disorderness of the probability distribution will be unreliable. For ideal AE entropy computation, the bin width range should be set close to the AE data acquisition systems resolution. The AE system used in this experiment was a 16-bit AMSY-6 system. For a 10 VDC range, it has a resolution of 0.000153 mV. Therefore, a bin width of 0.000153 was chosen for these tests.

In addition, it is worth noting that the present investigation was carried out in a controlled experimental

**Fig. 14** An AE waveform with a VDR of **a** – 10 to +10, **b** – 20 to +20, **c** – 40 to +40, **d** – 60 to +60, **e** – 80 to +80 and **f** – 100 to +100



environment, where the sensors were placed close to the damage source. In real condition monitoring of engineering structures using AE, a damage source may be located far away from the AE sensors and the AE signals would be subjected to attenuation and dispersion. Attenuation and dispersion is likely to affect the AE entropy value (as with all other traditional AE features). Moreover, noise generated from the grips and internal reflections within the test specimen were filtered out in these analysis. In real operational conditions, noise sources may be difficult to filter out and could bring difficulty in interpreting the damage using AE entropy. Further research needs to be carried out to investigate the effectiveness of AE entropy on complex engineering structures. Firstly, the effect of attenuation and dispersion on the calculated AE entropy needs to be understood. Secondly, the performance of AE entropy in noisy environments needs to be assessed.

## 5 Conclusion

The results show the potential of AE entropy to identify damage in the sample of 316L stainless steel subjected to fatigue loading. AE entropy of a signal is derived from its discrete amplitude distribution and is independent of acquisition settings, such as threshold and timing. A similar trend in AE cumulative entropy and AE features, such as count and energy, suggests that the traditional analysis can be replaced with AE entropy for critical damage identification as it is independent of acquisition settings and therefore reduces the need for human judgement in measuring the AE signal. The cumulative trend is consistent for the two tests performed. Moreover, it can be concluded that the sudden increase in AE entropy is generally an indication of critical damage, such as plastic zone formation as a result of growth and coalescence of micro-cracks; this would provide critical information to engineers monitoring a structure.

There are, however, a few important parameters to consider for AE entropy computation such as voltage VDR and bin width. Incorrect selection of these parameters will result in inaccurate AE entropy and may mask the signals generated from the damage mechanism. The influence of VDR can be avoided by setting it to the built-in maximum limit of the voltage range of the data acquisition equipment. The influence of bin width can be avoided by setting it close to the AE data acquisition systems resolution. Before the proposed parameter is implemented in the AE data acquisition system, more theoretical and experimental studies need to be conducted. Some important ones are: the effect of AE entropy due to the change of cracking mode; entropy due to the change in sample geometry; and the effect of dispersion on the calculated AE entropy.

**Acknowledgements** Funding was provided by Lloyd's Register Foundation.

## Compliance with ethical standard

**Conflict of interest** The authors declare that they have no conflict of interest.

**Open Access** This article is distributed under the terms of the Creative Commons Attribution 4.0 International License (<http://creativecommons.org/licenses/by/4.0/>), which permits unrestricted use, distribution, and reproduction in any medium, provided you give appropriate credit to the original author(s) and the source, provide a link to the Creative Commons license, and indicate if changes were made.

## References

1. Hellier CJ (2013) Handbook of nondestructive evaluation—(chapter 10). McGraw-Hill, New York
2. Mba D (2006) Development of acoustic emission technology for condition monitoring and diagnosis of rotating machines: bearings, pumps, gearboxes, engines, and rotating structures. *Shock Vib Dig* 38(1):3–16
3. Boller C (2012) Proceedings of the 6th European Workshop on SHM & 1st European Conference on PHM. Deutsche Gesellschaft für Zerstörungsfreie Prüfung, Berlin
4. Sinclair A, Connors D, Formby C (1977) Acoustic Emission during fatigue crack growth in steel. *Mater Sci Eng* 28(2):263–273
5. Berkovits A, Fang D (1995) Study of fatigue crack characteristic by acoustic emission. *Eng Fract Mech* 51(3):401–416
6. Fang D, Berkovits A (1995) Fatigue design model based on damage mechanism revealed by acoustic emission measurement. *ASME J Eng Mater Technol* 117(2):200–208
7. Roy H, Parida N, Sivaprasad S, Tarafder S, Ray K (2008) Acoustic emission during fracture toughness test of steel exhibiting varying ductility. *Mater Sci Eng A* 486(1–2):562–571
8. Han Z, Lou H, Cao J, Wang H (2011) Acoustic emission during fatigue crack propagation in a micro-alloyed steel and welds. *Mater Sci Eng A* 528(25–26):7751–7756
9. Han Z, Luo H, Zhang Y, Cao J (2013) Effects of micro-structure on fatigue crack propagation and acoustic emission behaviors in a micro-alloyed steel. *Mater Sci Eng A* 559:534–542
10. Shi S, Han Z, Liu Z, Valley P, Souza S, Kaewunruen S, Papaalias M (2018) Quantitative monitoring of brittle fatigue crack growth in railway steel using acoustic emission. *J Rail Rapid Transit* 232:1211–1224
11. Zhiyuan H, Hongyun L, Chuankai S, Junrong L, Mayorkinos P, Davis C (2014) Acoustic emission study of fatigue crack propagation in extruded AZ31 magnesium alloy. *Mater Sci Eng A* 597:270–278
12. Aggelis D, Kordatos E, Matikas T (2011) Acoustic emission for fatigue damage characterization in metal plates. *Mach Res Commun* 38(2):106–110
13. Roberts T, Talebzadeh M (2003) Fatigue life prediction based on crack propagation and acoustic emission count rate. *J Constr Steel Res* 59(6):679–694
14. Tanvir F, Sattar T, Mba D (2018) Identification of fatigue damage evolution in 316L stainless steel using acoustic emission and digital image correlation. In: Metec web of conference, Poitiers, France
15. Roberts T, Talebzadeh M (2003) Acoustic emission monitoring of fatigue crack propagation. *J Constr Steel Res* 59(6):695–712

16. Kohn D, Ducheyne P, Awerbuch J (1992) Acoustic emission during fatigue of Ti-6Al-4 V: incipient fatigue crack detection limits and generalized data analysis methodology. *J Mater Sci* 27(6):3133–3142
17. Pascoe J, Zarouchas D, Alderliesten R, Benedictus R (2018) Using acoustic emission to understand fatigue crack growth within a single load cycle. *Eng Fract Mech* 194:281–300
18. Barsoum F, Jamil S, Korcak A, Hill E (2009) Acoustic emission monitoring and fatigue life prediction in axially loaded notched steel specimen. *J Acoust Emiss* 27:40–63
19. Gagar D, Foote P, Irving P (2015) Effects of loading and sample geometry on acoustic emission generation during fatigue crack growth: implications for structural health monitoring. *Int J Fatigue* 81:117–127
20. Chai M, Zhang J, Zhang Z, Duan Q, Cheng G (2017) Acoustic emission studies for characterization of fatigue crack growth in 316LN stainless steel and welds. *Appl Acoust* 126:101–113
21. Xu D, Deniz E (2010) *Information theoretic learning*. Springer, New York, pp 47–102
22. Hartley R (1928) Transmission of information. *Bell Syst Tech J* 7:535–563
23. Shannon CE (1948) A mathematical theory of communication. *Bell Syst Tech J* 27:379–423–623–656
24. Renyi A (1960) On measures of entropy and information. In: *Proceedings of the 4th Berkeley symposium on mathematical statistics and probability*, vol 1, pp 457–561
25. Cornforth DJ, Tarvainen MP, Jelinek HFF (2014) How to calculate Renyi entropy from heart rate variability, and why it matters for detecting cardiac autonomic neuropathy. *Front Bioeng Biotechnol* 2:1–8
26. Coles PJ, Berta M, Tomamichel M, Wehner S (2017) Entropic uncertainty relations and their applications. *Rev Mod Phys* 89:015002
27. Bromiley P, Thacker N, Bouhova-Thacker E (2010) Shannon entropy, Renyi entropy, and information. *Tina Memo No. 2004-004: Statistics and Segmentation Series*
28. Vinga S, Almeida JS (2004) Renyi continuous entropy of DNA sequences. *J Theor Biol* 231:377–388
29. Zhang L, Cao Q, Lee J (2013) A novel ant-based clustering algorithm using Renyi entropy. *Appl Soft Comput* 13:2643–2657
30. Sluga D, Lotric U (2017) Quadratic mutual information feature selection. *Entropy* 19(4):157
31. Ekštejn K, Pavelka T (2014) Entropy and entropy-based features in signal processing. In: *Proceedings of PhD workshop systems & control, Balatonfured*
32. Vahaplar A, Çelikoğlu CC, Özgören M (2011) Entropy in dichotic listening EEG recordings. *Math Comput Appl* 16(1):43–52
33. Erdogmus D (2002) *Information theoretic learning: Renyi's entropy and its application to adaptive system training*. Ph.D. Thesis, University of Florida
34. Vijejan V, Hariharan M, Yaacob S, Nazri M, Sulaiman B, Adom A (2013) Objective investigation of vision impairments using single trial pattern reversal visually evoked potentials. *Comput Electr Eng* 39:1549–1560
35. Vijejan V, Hariharan M, Yaacob S (2014) Application of clustering techniques for visually evoked potentials based detection of vision impairments. *Biocybern Biomed Eng* 34:169–177
36. Chai M, Zhang Z, Duan Q (2018) A new qualitative acoustic emission parameter based on Shannon's entropy for damage monitoring. *Mech Syst Signal Process* 100:617–629
37. Chai M, Zhang Z, Duan Q, Song Y (2018) Assessment of fatigue crack growth in 316LN stainless steel based on acoustic emission entropy. *Int J Fatigue* 109:145–156
38. Sangid MD (2013) The physics of fatigue crack initiation. *Int J Fatigue* 57:58–72
39. Han KS, Oh KH (2006) Acoustic emission as a tool of fatigue assessment. *Key Eng Mater* 306–308:271–278
40. Ould Amer A, Gloanec A-L, Courtin S, Touze C (2013) Characterization of fatigue damage in 304L steel by an acoustic emission method. In: *5th Fatigue design conference, fatigue design*

**Publisher's Note** Springer Nature remains neutral with regard to jurisdictional claims in published maps and institutional affiliations.